



HAL
open science

A PERSPECTIVE ON DARCY'S LAW ACROSS THE SCALES: FROM PHYSICAL FOUNDATIONS TO PARTICULATE MECHANICS

Catherine O'Sullivan, Chloé Arson, Benoît Coasne

► **To cite this version:**

Catherine O'Sullivan, Chloé Arson, Benoît Coasne. A PERSPECTIVE ON DARCY'S LAW ACROSS THE SCALES: FROM PHYSICAL FOUNDATIONS TO PARTICULATE MECHANICS. *Journal of Engineering Mechanics - ASCE*, 2022, 10.1061/(asce)em.1943-7889.0002153 . hal-03821836

HAL Id: hal-03821836

<https://cnrs.hal.science/hal-03821836>

Submitted on 19 Oct 2022

HAL is a multi-disciplinary open access archive for the deposit and dissemination of scientific research documents, whether they are published or not. The documents may come from teaching and research institutions in France or abroad, or from public or private research centers.

L'archive ouverte pluridisciplinaire **HAL**, est destinée au dépôt et à la diffusion de documents scientifiques de niveau recherche, publiés ou non, émanant des établissements d'enseignement et de recherche français ou étrangers, des laboratoires publics ou privés.

A PERSPECTIVE ON DARCY'S LAW ACROSS THE SCALES: FROM PHYSICAL FOUNDATIONS TO PARTICULATE MECHANICS

Catherine O'Sullivan¹, Chloé Arson², and Benoît Coasne³

¹Department of Civil and Environmental Engineering, Imperial College London, UK.

Email: cath.osullivan@imperial.ac.uk

²School of Civil and Environmental Engineering, Georgia Institute of Technology, USA

³Université Grenoble Alpes, CNRS, LIPHY, France

ABSTRACT

This paper puts forward a perspective or opinion that we can demonstrate Darcy's law is valid at any scale where fluid can be modelled/analyzed as a continuum. Darcy's law describes the flow of a fluid through a porous medium by a linear relationship between the flow rate and the pore pressure gradient through the permeability tensor. We show that such a linear relationship can be established at any scale, so long as the permeability tensor is expressed as a function of adequate parameters that describe the pore space geometry, fluid properties and physical phenomena. Analytical models at pore scale provide essential information on the key variables that permeability depends on under different flow regimes. Upscaling techniques based on the Lippman-Schwinger equation, pore network models or Eshelby's homogenization theory make it possible to predict fluid flow beyond the pore scale. One of the key challenges to validate these techniques is to characterize microstructure and measure transport properties at multiple scales. Recent developments in imaging, multi-scale modeling and advanced computing offer new possibilities to address some of these challenges.

NOTATION

- a' and a'' constants in Darcy-Forcheimer law

- 23 • A cross sectional area
- 24 • $\mathbf{A}(\mathbf{x})$ localization tensor
- 25 • b slip length
- 26 • b_0 system dependant constant
- 27 • C constant of integration
- 28 • c sound velocity (scalar) in fluid
- 29 • CNNs Convolutional Neural Networks
- 30 • D diameter
- 31 • D_0 collective diffusivity
- 32 • DPD dissipative particle dynamics
- 33 • FVM Finite Volume Method
- 34 • FD finite difference
- 35 • \mathbf{g} acceleration due to gravity
- 36 • G_{ab} hydraulic conductance of throat connecting pores a and b
- 37 • \mathbf{J} flux
- 38 • $j_x(\mathbf{k}, t)$ Fourier component of the flow velocity
- 39 • \mathbf{k} permeability tensor
- 40 • $\mathbf{k}(\mathbf{x})$ local permeability tensor
- 41 • \mathbf{K} permeance tensor
- 42 • \mathbf{K}' hydraulic conductivity
- 43 • K_{ab} intrinsic conductance
- 44 • k_B Boltzmann's constant
- 45 • Kn Knudsen number
- 46 • L measure of length
- 47 • LBM Lattice Boltzman Method
- 48 • LSTM Long-Short-Term-Memory
- 49 • Ma Mach number

- 50 • MD molecular dynamics
- 51 • n porosity
- 52 • NMR nuclear magnetic resonance
- 53 • N_p number of adjacent pores
- 54 • P pressure
- 55 • \bar{P} average pressure
- 56 • PFGNMR pulsed field gradient nuclear magnetic resonance
- 57 • Q flow rate
- 58 • Q_{ab} flow rate from pore a to pore b
- 59 • QENS quasielastic neutron scattering
- 60 • r radial direction origin at centre of cylinder
- 61 • Re Reynolds number
- 62 • REV Representative Elementary Volume
- 63 • s specific surface area of system
- 64 • SPH smooth particle hydrodynamics
- 65 • t time
- 66 • \mathbf{v} velocity field
- 67 • $\bar{\mathbf{v}}$ average flow rate
- 68 • $\bar{\mathbf{v}}_s$ seepage velocity
- 69 • η fluid viscosity
- 70 • λ mean free path length
- 71 • ξ friction between the flowing fluid and solid
- 72 • ρ fluid density
- 73 • σ kinetic diameter
- 74 • $\sigma_{\alpha\beta}$ stress tensor component
- 75 • τ_R stress relaxation time in the fluid particle
- 76 • τ fluid momentum transfer time

INTRODUCTION

In his pioneering work on city fountains in Dijon (France), Henry Darcy established an experimental relationship in which the average flow rate \bar{v} is proportional to the pressure drop, ΔP , inducing the flow (Darcy, 1856). When Darcy's law is used in civil engineering applications, the flow rate is usually expressed in terms of a gradient of the total head, i.e. as:

$$\bar{\mathbf{v}} = -\frac{\mathbf{k}}{\eta} \cdot (\nabla P - \rho \mathbf{g}) \quad (1)$$

where \mathbf{k} is the permeability (sometimes termed the *intrinsic permeability*), ∇P is the gradient in pressure, the vector \mathbf{g} represents acceleration due to gravity, ρ is the fluid density, and η is the fluid viscosity under given pressure/temperature conditions. In Eq. 1, the parameter \mathbf{k} relates two vector quantities and so it is a tensor denoted k_{ij} . The unit of (intrinsic) permeability is the darcy, 1 darcy = $9.869233 \times 10^{-13} m^2$ or $0.9869233 \mu m^2$. In geotechnical engineering, where Darcy's law is expressed in terms of a gradient in the total head (energy/unit weight) and the permeating fluid is usually water the term permeability (with units of m/s) is generally used for $\mathbf{K}' = \mathbf{k}\rho g/\eta$ (Cashman and Preene, 2021); arguably for clarity and precision the term *hydraulic conductivity* should be used for \mathbf{K}' when water is the permeating fluid. The term *permeance* is used to designate the quantity $\mathbf{K} = \mathbf{k}/\eta$, which is not restricted to water as the permeating fluid. Typical values of \mathbf{K}' for geomaterials are given in Table 1.

The simple, linear relationship that is Darcy's law, is applied in physics and chemistry, materials and Earth sciences, mechanical and chemical engineering, soil and agricultural sciences, etc. In civil engineering, Darcy's Law is routinely used in geotechnical engineering design and analysis, including but not limited to the design of dewatering systems to control ground water during construction (Cashman and Preene, 2021) and seepage analysis to design and assess levee systems (Smith et al., 2013). Darcy's law is also applied when interpreting well pumping tests to assess hydraulic conductivity in situ. Even though Darcy's law was historically introduced empirically 150 years ago, it was fully justified within the theoretical framework of homogenization at the

102 scale of continua at the end of the twentieth century (e.g., Boutin et al. (2010)). However, with the
103 emergence of nanoscience, many fundamental questions have been raised regarding the validity of
104 Darcy's law at vanishing length scales. In particular, considering that the flowing fluid can no longer
105 be treated as a continuum medium at the nanometer scale, many poorly known phenomena become
106 important as the molecular nature of the fluid comes into play (Bocquet and Charlaix, 2010).
107 At the same time, questions about Darcy's law have been put forward in the civil engineering
108 literature. For example, Hansbo (2001) has argued that Darcy's law is not valid in clay at low
109 hydraulic gradients. Ejezie et al. (2021) have highlighted the challenges associated with applying
110 Darcy's law to predict the behaviour of non-Newtonian polymer fluids in sand, an application that
111 is important to develop effective support for deep excavations.

112 Recent developments in numerical analysis and imaging, alongside an emerging emphasis on
113 multi-scale analysis, allow us to re-examine Darcy's law. In this paper, we explore how we can bridge
114 our understanding of flow at different scales within the framework of Darcy's law. Three questions
115 underpin this discussion: (1) How can we establish the validity of Darcy's law at multiple scales? (2)
116 What mechanisms underlie the regimes where Darcy's law fails to capture the relationship between
117 the flow rate and the pressure gradient? (3) How can we upscale permeability from fundamental
118 measures of porous media? This contribution adopts a fundamental perspective. It does not address
119 key issues in engineering practice such as challenges associated with measuring permeability in
120 situ or in the laboratory. However, the insight emerging from the detailed consideration of the
121 nature of fluid flow in porous media can underpin practical analyses and interpretation of in situ
122 observations.

123 In this contribution we explore the general applicability of Darcy's law by considering flow
124 in a single, cylindrical pore for different scenarios, including non-laminar flow and non-advective
125 flow. This abstract model provides us with a clear basis to understand some of the limitations of
126 the applicability of Darcy's law and we take it a basis to reflect on how to extend Darcy's law to
127 poromechanical problems that involve strong couplings with chemical and physical processes that
128 occur at the pore scale and below. We distinguish between analysis of fluid at the molecular and

129 continuum scales and show that, once water can be modelled as a continuum, Darcy’s law is valid
130 at all scales so long as the permeability is expressed as the correct function of geometric, chemical,
131 physical and mechanical parameters that fluid flow depends on.

132 **VALIDITY OF DARCY’S LAW AT MULTIPLE SCALES**

133 Considerations of scale must be addressed in even the most basic analysis of Darcy’s law. The
134 term \bar{v} in Eq. 1 refers to a flow rate, Q , divided by a cross sectional area, A , orthogonal to the
135 direction of flow, i.e. $\bar{v}_i = Q_i/A$. The term \bar{v} is sometimes referred to as the Darcy flux or Darcy
136 velocity (Cashman and Preene, 2021) or the discharge velocity (Cedergren, 1997). The area, A ,
137 is occupied by both pore space and solid space, and so, clearly, without considering any local or
138 global heterogeneities, the term \bar{v} in Darcy’s law is not the velocity of fluid flow. Mitchell and
139 Soga (2005) and Cashman and Preene (2021) refer to \bar{v} as an apparent velocity; \bar{v} can also be seen
140 as “a statistical summary of viscous flow” (Ineson, 1956). The actual pore water flow velocity
141 will always differ from \bar{v} . The mean pore velocity is given by $\bar{v}_s = \bar{v}/n$ (where n is the porosity)
142 and is termed the average linear groundwater velocity (Cashman and Preene, 2021) or the seepage
143 velocity (Cedergren, 1967).

144 **Sub-pore scale - numerical models**

145 Modern numerical and experimental techniques enable us to consider the details of fluid flow
146 in the pore space. At the molecular level, the arrangement of water in the pore space can be
147 highly complex due to mechanisms including multi-layer adsorption, surface hydration and cation
148 hydration (e.g. Zhang and Lu (2018); Coasne (2016)). As illustrated schematically in Figure 1 (a),
149 water in the pore space can be studied by molecular models using either Molecular Dynamics or
150 Monte Carlo simulations with an appropriate water model (e.g. Pathirannahalage et al. (2021)).
151 The insight provided by considering these molecular mechanisms can inform our understanding of
152 fluid flow in porous media. The exact dimension/resolution at which the continuum assumption
153 applies depends on the fluid in question, the temperature and the pressure; for any fluid the
154 continuum-discrete limit is approximately between 1nm and a few nm. As discussed in (Bocquet

155 and Charlaix, 2010), this limit can be determined from the correlation time of the stress-strain
156 correlation function.

157 When the fluid is viewed as a continuum, direct simulation of fluid flow in the pore space can be
158 achieved if the 3D topology of the pore space is available. This 3D topology data can be obtained
159 from numerical simulations using the discrete element method (e.g. Knight et al. (2020), Zhao
160 and O’Sullivan (2022)), laser scanning of transparent soil (e.g. Sanvitale et al. (2022)), or micro
161 computed tomography scanning (e.g. Talon et al. (2012); Blunt et al. (2013); Taylor et al. (2015);
162 Sun and Wong (2018)). The particle surfaces are taken as boundaries to the fluid flow. In this type
163 of model, rather than considering Darcy’s law, the Navier-Stokes equations are solved numerically
164 using, for example, the finite volume method (FVM) (Figure 1 (b)). The Lattice-Boltzmann Method
165 (LBM) which solves Boltzmann’s transport equation by introducing a lattice discretization can also
166 be used (Figure 1 (c)). Whether the LBM or the FVM method is used, assumptions must be
167 made regarding the boundary condition that is applied at the fluid-particle interface; typically a
168 no-slip boundary condition is applied. In this context, it is important to realize that these methods
169 implicitly or explicitly assume some specific regimes which often fail to capture the complexity of
170 fluid dynamics in the vicinity of the surface (slippage, adsorption, non-viscous effects including
171 memory effects, etc.). Some of these aspects will be covered in the next section. An additional key
172 challenge in performing continuum simulations such as FVM or LBM is meshing the often complex
173 topology of the pore space. The computational cost of the simulations restricts considerations to
174 relatively small sub-volumes, however experimental work has shown that despite the resultant
175 boundary effects, this type of model can capture the details of fluid flow with reasonable accuracy
176 (Sanvitale et al., 2022). Results from these simulations can inform our understanding of Darcy’s
177 law at the macro-scale. While Darcy’s law does not emerge from these models, they allow us to
178 estimate the permeabilities (i.e. the proportionality constant between the flow and the pressure
179 drop inducing the flow) for different thermodynamic and hydrodynamic regimes. In particular, by
180 post-processing the fluid velocity field, one can calculate the overall permeability of an assembly of
181 particles with a complex pore topology (e.g. Taylor et al. (2017)) or the conductance that governs

182 flow in an individual pore throat (e.g. Sufian et al. (2019)). As discussed below, homogenization
 183 approaches can be applied.

184 **Sub-pore scale - analytical models**

185 While useful insight can be gained from numerical models that operate at the sub-pore scale,
 186 analytical models have the advantage of developing closed-form expressions where the relationships
 187 between key variables are explicit. By assuming that the pressure gradient inducing transport
 188 is small enough for the flow to be laminar, viscous and incompressible, Poiseuille-Hagen flow
 189 equations can be applied in media with simple pore network shapes (morphology/topology).

190 In what is perhaps the simplest scenario, we consider a cylindrical pore of length L and diameter
 191 D filled with an incompressible fluid having a (constant) viscosity η and subjected to a pressure
 192 gradient ∇P . For small Reynolds numbers, the flow can be assumed to be laminar as inertial
 193 contributions $\mathbf{v} \cdot \nabla \mathbf{v}$ (where \mathbf{v} is the velocity field) are negligible. In this case, the Navier-Stokes
 194 equation for momentum conservation reads (Bird et al., 2002):

$$195 \quad \rho \frac{\partial \mathbf{v}}{\partial t} = -\nabla P + \eta \nabla^2 \mathbf{v} \quad (2)$$

196 For steady-state (stationary) conditions where $\partial \mathbf{v} / \partial t = 0$, the equation reduces to $\nabla P = \eta \nabla^2 \mathbf{v}$.
 197 Taking x to be the direction of the pressure gradient, i.e. $\nabla P_x = -\Delta P / L$, and r as the radial direction
 198 with origin at the centre of the cylinder, one obtains a velocity field $\mathbf{v} = v_x(r) \mathbf{e}_x$ (where \mathbf{e}_x is a unit
 199 vector in the x direction). Integrating twice with respect to x leads to $v_x(r) = -\Delta P r^2 / 2L\eta + C$
 200 where the constant C is calculated from the velocity boundary condition imposed by solid surface.
 201 Macroscopically, this boundary condition at the pore surface usually corresponds to a “no slip”
 202 condition so that $v_x(r = D/2) = 0$ and hence $C = \Delta P / 8L\eta \times D^2$ (as discussed in the previous
 203 section, this no-slip boundary condition is usually assumed to be valid, without further justification,
 204 in mesoscopic approaches such as FVM and LBM). In turn, this leads to the following velocity
 205 profile for a cylindrical pore:

$$206 \quad v_x(r) = \frac{\Delta P D^2}{16L\eta} \left[1 - \left(\frac{2r}{D} \right)^2 \right] \quad (3)$$

207 Hence, as illustrated in Figure 2, at any given position, r , there is a linear dependency of the velocity
 208 $v_x(r)$ upon the pressure gradient, $\Delta P/L$. The latter equation allows deriving the average velocity
 209 over the whole cross-section area ($\bar{v} = \Delta PD^2/32\eta L$) and the maximum velocity in the pore center
 210 ($v_{\max} = \Delta PD^2/16\eta L$).

211 The velocity boundary condition imposed by the solid surface depends on the detailed fluid/solid
 212 wetting properties and the structure of the solid surface. Under significant wetting, the large
 213 fluid/solid interactions lead to no-slip conditions and the velocity vanishes at the pore surface,
 214 leading to Eq. 3. In contrast, for partial wetting, the fluid slips at the pore surface with a velocity
 215 field that does not vanish when $2r \rightarrow D$. In this case, the so-called slip length b corresponds to the
 216 distance at which the linearly extrapolated velocity vanishes, i.e. $-b\partial v_x/\partial r = v_x$ (see Figure 2.b
 217 over the length of b). When this boundary condition is applied, the constant obtained following
 218 double integration becomes $C = \Delta PD^2/16L\eta \times [1 + 4b/D]$, giving the following velocity profile:

$$219 \quad v_x(r) = \frac{\Delta PD^2}{16L\eta} \left[1 + \frac{4b}{D} - \left(\frac{2r}{D} \right)^2 \right] \quad (4)$$

220 When compressible fluids are considered (e.g. gases, supercritical fluids, etc.), special attention
 221 should be paid as to whether or not the flow can be treated as incompressible. Flow can be classified
 222 as compressible or incompressible by considering the dimensionless Mach number, defined as
 223 $\text{Ma} = v/c$, where c is the sound velocity in the fluid and v can be taken as the maximum velocity.
 224 For $\text{Ma} < 0.3$, the fluid flow can be regarded as incompressible because the flow is not affected
 225 by the pressure wave induced upon fluid displacement. On the other hand, for $\text{Ma} > 0.3$, fluid
 226 compressibility affects the flow and the Hagen-Poiseuille flow provided above must be modified.
 227 Compressible flow behaves with an apparent slip length, b , defined as $v_x = -b\partial v_x/\partial r$, as before,
 228 however the slip length b scales with the inverse of the pressure, i.e. $b = b_0/\bar{P}$, where b_0 is a
 229 system-dependent constant while \bar{P} is the average pressure between the upstream and downstream
 230 pressures. The velocity profile for such a compressible flow in a cylindrical pore of diameter D can

231 then be expressed as (Bird et al., 2002):

$$232 \quad v_x(r) = \frac{\Delta P D^2}{16 L \eta} \left[1 + \frac{4 b_0}{D \bar{P}} - \left(\frac{2r}{D} \right)^2 \right] \quad (5)$$

233 This equation corresponds to the so-called Klinkenberg effect which can describe flow that is an
234 intermediate regime between Knudsen diffusion and viscous flow. As expected, for large pressures
235 \bar{P} , the fluid becomes incompressible so that slippage effects captured in b_0/\bar{P} vanish and Eq. 5
236 becomes equivalent to the Poiseuille flow predicted under the no-slip hypothesis (Eq. 3).

237 Both Eq. 3 and 4 predict a linear relationship between $v_x(r)$ and $\Delta P/L$ for incompressible flow
238 whether or not there is slip at the fluid-solid interface. While it may appear that Eq. 5 again gives a
239 linear relationship between $v_x(r)$ and $\Delta P/L$ for incompressible flow, the situation is more complex
240 as the constant of proportionality depends upon \bar{P} as well as upon the pressure variations $P(x)$
241 along the pore length L . However, in most situations, provided the pressure variations are smooth,
242 one can write $P(x) \simeq \bar{P} + x \nabla P$ where ∇P is essentially constant so that the proportionality factor
243 in Eq. 5 only depends on \bar{P} and ∇P .

244 **Upscaling from the Hagen-Poiseuille equations**

245 The Hagen-Poiseuille equations above were derived for a simple pore geometry so that a well-
246 defined velocity boundary condition can be imposed. When considering more realistic materials,
247 a more complex porous volume geometry must be used. Using the same linear response regime
248 formalism and assuming the fluid flow to be incompressible and purely advective, the Hagen-
249 Poiseuille equation can be extended to any real medium.

250 For ideal pore geometries such as slit and cylindrical pores, the permeability \mathbf{k} can be inferred
251 by mapping Darcy's law onto the corresponding Poiseuille flow. For a porous medium with a
252 porosity n , the flux $\mathbf{J} = \rho \bar{\mathbf{v}}$ is given by:

$$253 \quad \mathbf{J} = -\frac{\rho n \mathbf{k}}{\eta \tau} \cdot \nabla P \quad (6)$$

254 where the dimensionless factor τ is coined as tortuosity. This parameter ensures that Eq. 6 holds

255 when relating the observed flow J to the other physical constants that appear in the equation.
256 In practice, this tortuosity correction accounts for several effects that pertain either to the pore
257 network geometry (e.g. flow paths that depart from a straight line, non-cylindrical pore shapes) or
258 adsorption and surface phenomena (e.g. complex pore surface hydrodynamic boundary, residence
259 times).

260 A particular form of Darcy's law is obtained when using the Kozeny-Carman relation for 1D
261 flow in which permeability is a scalar noted k which is a function of the geometry of the porous
262 space. Using the specific surface area of the system s , the Kozeny-Carman relation writes:

$$263 \quad k = \frac{1}{5s^2} \times \frac{n^3}{1-n^2} \sim \frac{D^2}{180} \times \frac{n^3}{1-n^2} \quad (7)$$

264 where the second equality corresponds to the situation of spherical pores having a size D so that
265 $s = 6/D$. The Kozeny-Carman expression of permeability is used when applying Darcy's law
266 to reflect the effect of porosity, pore size and pore shape (tortuosity) on permeability. In other
267 words, the Kozeny-Carman model gives an estimate of the effective permeability based on simple
268 descriptors of the microstructure. Thus, it is not generalizable to all porous media.

269 **WHEN IS FLUID FLOW NOT A LINEAR FUNCTION OF THE GRADIENT OF PRESSURE?**

270 Darcy's law is a linear response equation which can be seen as a specific expression of Onsager's
271 phenomenological theory of transport applied to fluid flow in a porous medium (Onsager, 1931;
272 Barrat and Hansen, 2003). Darcy's linear equation has proven to accurately describe laminar flow
273 at several scales. This section reviews cases when the relationship between fluid flow is not a linear
274 function of the gradient of pressure, including well-known problems of turbulent flow, gas flow,
275 and fluid slippage along the pore boundaries.

276 **Non laminar flow**

277 It is expected that Darcy's law will apply only for a small Reynolds number Re ($Re < 10$, where
278 $Re = \rho v D / \eta$ with ρ the fluid density, v the flow rate, D the characteristic pore size and η the fluid
279 dynamic viscosity). In the case of larger Reynolds numbers, this approximation no longer holds and

280 quadratic terms in the flow rate must be added to Darcy's equation. In what follows, we consider
281 1D flow for the sake of simplicity but the description can be extended to 3D anisotropic systems:

$$282 \quad -\nabla P \sim a'\bar{v} + a''\bar{v}^2 \quad (8)$$

283 where a' and a'' are constants. Physically, Eq. 8 accounts for non-linear effects as turbulence
284 arises upon increasing Re. When such effects are included in Darcy's law, one obtains the so-called
285 Darcy-Forchheimer law (Nield and Bejan, 2006):

$$286 \quad -\frac{k}{\eta} \cdot \nabla P = \bar{v}(1 + b'\bar{v}) = \bar{v}(1 + b''\text{Re}) \quad (9)$$

287 where the second equality on the right-hand side is derived by using $\text{Re} = \rho v D / \eta$ (b' and b'' are
288 constants).

289 **Transition from advective to diffusive flow**

290 The assumption of advective flow is central to the derivation of Darcy's law. Depending on the
291 flowing fluid – i.e. liquid, gas, supercritical fluid, the flow can be incompressible or compressible
292 with underlying transport mechanisms of varying complexity that strongly depend on the applied
293 thermodynamic boundary limits. In many situations relevant to practical applications, the flow rate
294 complexity is a consequence of the dependence of the local density at a given position in the porous
295 medium on the local pressure.

296 Knudsen diffusion corresponds to situations where fluid transport mostly occurs through diffu-
297 sion of molecules colliding with pore walls as the fluid mean free path far exceeds the pore size.
298 In general, fluid transport in porous media can be rationalized by considering its mean free path
299 $\lambda \sim 1/\rho\sigma^2$ where ρ and σ are the fluid density and kinetic diameter, respectively (typically, σ is a
300 fluid-specific quantity related to the scattering cross-section, which represents the probability that
301 a molecule collides with another). For compressible phases such as gases or supercritical fluids,
302 λ depends strongly on the applied pressure with values that can be either close to the pore size D
303 (“tight gas”) or very large compared to D (infinite dilution). The Knudsen number $\text{Kn} = \lambda/D$ is

304 the appropriate dimensionless number to describe the flow type as a function of λ . Depending on
305 the Knudsen number characterizing the flow, different regimes that deviate from Darcy's law can
306 be encountered, as summarized here (Ziarani and Aguilera, 2012; Bear, 2018):

307 **Viscous flow, $Kn < 0.01$.** In this asymptotic regime, the flow is advective as described using Darcy's
308 law. In this case, the flowing fluid is in the laminar regime (i.e. low Re).

309 **Slip flow, $Kn \sim [0.01 - 0.1]$.** In this regime, the flow obeys Darcy's law corrected for Klinkenberg
310 effect. As discussed above, this correction corresponds to compressibility-induced slippage at the
311 solid surface.

312 **Transition flow, $Kn \sim [0.1 - 10]$.** This transition regime corresponds to complex transport mecha-
313 nisms where advection and diffusion are combined. Under such regimes, these two contributions
314 sum up, as advection and diffusion occur in parallel (Kärger et al., 2012). Upon increasing Kn, the
315 flow evolves in a continuous fashion from purely advective to purely diffusive.

316 **Knudsen diffusion, $Kn > 10$.** In this asymptotic domain, the fluid mean free path largely exceeds
317 the pore size so that Knudsen diffusion prevails with an underlying transport mechanism governed
318 by molecular collisions with the solid surface.

319 **Deviation from Darcy's law at the nanoscale**

320 Adsorption effects can drastically affect the permeability and lead to a complex dependency of
321 \mathbf{k} on fluid density i.e. $\mathbf{k}(\rho)$. Where this arises, upon imposing a pressure gradient across a porous
322 medium to induce fluid transport, non linear effects are expected. This departure from Darcy's
323 law stems from the strong adsorption at the pore surface. As explained in (Falk et al., 2015), these
324 molecular effects make the viscous flow approximation at the heart of Darcy's law invalid. Without
325 going too much into details, for fluid flow in a porous medium, Stokes' equation for momentum
326 conservation in a laminar flow writes:

$$327 \quad \rho \frac{\partial \mathbf{v}}{\partial t} = -\nabla P + \eta \nabla^2 \mathbf{v} - \xi \mathbf{v} \quad (10)$$

328 where ξ is the friction between the flowing fluid and the solid. Writing this conservation relation in
 329 Fourier space in a direction x normal to the flow direction gives the following differential equation
 330 $\partial j_x(\mathbf{k}, t)/\partial t = (-\eta k^2/\rho - \xi)j_x(\mathbf{k}, t)$ where $j_x(\mathbf{k}, t)$ is the Fourier component of the flow velocity.
 331 Assuming for the sake of simplicity isotropic flow, the general solution of this differential equation
 332 is given by:

$$333 \quad \langle j_x(k, t)j_x(-k, 0) \rangle \sim \exp \left[\left(\frac{-\eta k^2}{\rho} - \xi \right) t \right] \quad (11)$$

334 We note that the latter equation does not involve the pressure gradient because such time correlation
 335 functions are probed in the direction normal to the flow (i.e. perpendicular to the pressure gradient).
 336 As illustrated in (Falk et al., 2015), in some cases, velocity fluctuations for nanoconfined fluids
 337 do not follow the behavior expected according to Eq. 11. This indicates that in such extreme
 338 confinement, the flow is not simply viscous as assumed in Darcy's equation. In this case, memory
 339 effects as defined in generalized hydrodynamics have to be taken into account.

340 Bocquet and Charlaix (2010) provide an explanation for the viscous flow approximation break-
 341 down, which is summarized here. Continuum conservation laws such as Stokes' equation assume
 342 a time scale separation between the stress relaxation time τ_R inside the fluid particle and the fluid
 343 momentum transfer time τ . On the one hand, stress relaxation within the fluid occurs over a typical
 344 time given by the time correlations in the stress tensor since $\eta = 1/Vk_B T \int \sigma_{\alpha\beta}(t)\sigma_{\alpha\beta}(0)dt$; in
 345 this equation, $\sigma_{\alpha\beta}$ is the stress tensor component with $\alpha, \beta = x, y, \text{ or } z$. This expression, known
 346 as Green-Kubo formula for the viscosity, can be derived in the framework of the linear response
 347 theory (Barrat and Hansen, 2003). In the specific context of viscosity, this equation indicates
 348 that the viscosity characterizes how fast the stress relaxes in the fluid particle (here, "particle" is
 349 understood in the context of hydrodynamics so that it corresponds to a small fluid element/volume
 350 in which the fluid can be treated as a continuum medium). Typically, the relaxation time τ_R for
 351 the stress tensor is of the order of 10^{-12} s even if the value can vary broadly depending on fluid
 352 molecular nature, temperature, density, etc. On the other hand, momentum transfer occurs over a
 353 characteristic time given by the decay time in the correlation function (Barrat and Hansen, 2003):
 354 $\langle j_x(k, t)j_x(-k, 0) \rangle \sim \exp[-t/\tau]$ with $\tau = (k^2\rho/\eta - \xi)^{-1}$. In the continuum (macroscopic) limit,

355 there is a marked time scale separation between these different phenomena as $k \rightarrow 0$, $\tau_R \ll \tau$. In
356 contrast, in extreme confinement and/or with strong surface adsorption effects, momentum transfers
357 occur with wave vectors $k \sim 1/D$ where D is the pore size. As explained in (Bocquet and Charlaix,
358 2010), for such ultra-confined fluids, time scale separation is no longer valid as $\tau_R \sim \tau$.

359 From a practical viewpoint, the viscous breakdown does not render Darcy's law invalid in the
360 sense that proportionality between the flow rate and gradient pressure is still observed. However,
361 strong molecular effects such as adsorption lead to permeabilities that are no longer an intrinsic
362 property of the host porous medium. In particular, the permeability becomes a complex quantity
363 that depends on both the solid and fluid properties as well as on the details of their interaction.

364 **Permeability and Permeance**

365 While Darcy's law can almost always be used empirically, the challenge in expressing per-
366 meability as a function of solid and fluid properties raises questions regarding the concept of
367 permeability as a robust physical descriptor for flow in complex porous media. There are es-
368 sentially two scenarios where the assumptions of viscous flow and ideal pore geometry become
369 questionable: (1) For disordered pore morphology and pore network topology, regardless of the
370 pore size, the permeability can no longer be written as a simple function of the pore size as the
371 complex geometry does not make it possible to write well-defined boundary conditions. (2) In
372 extreme confinement, such as in nanoporous media, the complex thermodynamics of the fluid in
373 the vicinity of the solid surface is strongly coupled with the hydrodynamic flow. The permeability
374 becomes a complex function of the fluid local properties (e.g., density, adsorption, dynamics).
375 In very small pores, where the fluid molecular granularity can no longer be ignored, additional
376 questions arise regarding, for instance, the validity of macroscopic concepts such as viscosity.

377 While it is often assumed that k only depends on the porous solid properties (typically, the pore
378 size D and/or specific surface area s), there is significant experimental evidence for complex perme-
379 ability changes upon varying the fluid, density, temperature, etc. These effects were discussed by
380 Falk et al. (2015) who considered hydrocarbon transport (e.g. methane, propane, hexane, nonane,
381 and dodecane) in a disordered nanoporous solid. Falk et al. found that the flow varies linearly

382 with the prescribed pressure gradient *i.e.* $\mathbf{J} \sim \nabla P$ and that the permeability k depends on the fluid
383 molecule as well as on the fluid density. The concept of permeability can encompass both geomet-
384 rical effects (tortuosity, morphology), physical/chemical effects (e.g. adsorption) and mechanical
385 effects (non viscous effects, necking, etc.) (Coasne, 2016). Due to the intrinsic complexity of these
386 combined effects, additional phenomena occur at different scales (e.g. adsorption-induced porome-
387 chanical effects, memory effects in fluid flow, thermodynamical and dynamical phase transitions).
388 As a result, attempts to use theories including those relying on computational fluid dynamics tools
389 may fail to establish robust expressions for the fluid permeability in a given porous medium. Com-
390 bined geometric, chemical, physical and mechanical effects started to receive full attention with the
391 advent of nanoporous materials (especially in the context of nanofluidics), but they are expected to
392 apply to almost all practical situations as they are intrinsically linked to the thermodynamics and
393 dynamics of confined and/or interfacial fluids.

394 As mentioned above, Darcy's law can be expressed using a single parameter $\mathbf{K}' = \mathbf{k}\rho g/\eta$
395 known as hydraulic conductivity or $\mathbf{K} = \mathbf{k}/\eta$ known as permeance. The expression $\mathbf{K}' = \mathbf{k}\rho g/\eta$
396 implies that permeability \mathbf{k} is an intrinsic property of the host porous material and that the use
397 of a single hydraulic conductivity parameter \mathbf{K}' couples the intrinsic properties of the fluid and
398 solid. The same is true of the permeance $\mathbf{K} = \mathbf{k}/\eta$ defined from momentum balance equations.
399 For example, using molecular modeling, Falk et al. (2015) and later Obliger et al. (2016) showed
400 that the 1D flow of different hydrocarbons (density, chain length) in disordered nanoporous solids
401 cannot be reconciled with Darcy's law expressed as $v_x/\nabla P = k/\eta$. On the other hand, the flow
402 of confined molecules was found to be linearly related to the pressure gradient *i.e.* $\bar{v} \sim -K\nabla P$.
403 The permeance K is a complex function of the fluid density and molecule type. Yet, as expected
404 for an incompressible fluid, the permeance was found to be consistent (Falk et al., 2015) with the
405 so-called collective diffusivity $D_0 = K\rho k_B T$ where D_0 is defined as Onsager's transport coefficient
406 associated with the chemical potential gradient: $J = \rho\bar{v} = -[\rho D_0/(k_B T)] \nabla\mu$. This expression
407 can be recovered by using Gibbs-Duhem equation at constant temperature, *i.e.* $\rho d\mu = dP$.

408 The analogy between the permeance and collective diffusivity – albeit established for an in-

409 compressible fluid – is an important cornerstone as it provides a means to estimate the permeance
410 of a medium without performing sometimes complex permeability measurements. Of particu-
411 lar relevance, the collective diffusivity can be assessed using neutron scattering techniques with
412 deuterated liquids (in contrast to hydrogen, deuterium is a strong neutron coherent scatterer which
413 allows probing the collective part of the dynamical structure factor). A key advantage of such
414 experiments over permeability measurements is that they are performed under no flow conditions
415 – i.e. fluid at rest – as the fluctuation-dissipation theorem allows linking the transport coefficient
416 (collective diffusivity here) to fluctuations in a given microscopic quantity (center of mass velocity
417 here) through the Green-Kubo formalism. This central framework in statistical mechanics allows
418 one to relate any transport quantity to fluctuations in microscopic variables (Mc Quarrie, 2000). Of
419 particular interest for fluid transport in confined media, it can be shown (Barrat and Hansen, 2003)
420 that the self-diffusivity is directly given by the time integral of the time autocorrelation function of
421 the individual velocities (i.e. $\langle v(t)v(0) \rangle$) while the collective diffusivity is given by the integral of
422 the time autocorrelation of the center-of-mass velocities (i.e. $\langle v_{\text{COM}}(t)v_{\text{COM}}(0) \rangle$).

423 **UPSCALING PERMEABILITY**

424 Despite decades of intense research by engineers and physicists, rigorous structure-property
425 relations that link permeance (or hydraulic conductivity) and variables (fluid and material properties,
426 thermodynamic conditions) for a given system are still lacking. In practice, the development of
427 accurate and practical relationships has been hampered by the fact that the different communities
428 interested in these issues often work independently from each other. On the one hand, researchers
429 working on complex porous media such as in engineering fields mostly use Darcy’s equation in an
430 empirical fashion while trying to use reverse-engineering approaches to relate the microstructure of
431 the porous medium to the flow properties observed in its pore space. On the other hand, researchers
432 working in more basic science fields usually employ simpler porous media (ideally close to simple
433 geometry channels) in combination with microscopic formalisms from statistical physics to unravel
434 the complexity of fluid flow in confinement or near surfaces at the microscopic scale.

Engineering approaches: upscaling from pore scale

Full-field methods

Geomaterials contain solid grains and pore spaces of heterogeneous shapes, sizes and orientations. In full-field methods, features of the microstructure such as grains and pores are discretized in space, and field variables such as displacement, stress, pore pressure and porosity change are calculated at each point of the discretization grid. Composite materials were successfully simulated with the Finite Element Method (FEM), by discretizing each feature of the microstructure with several volume elements, so as to reproduce the spatial distribution of the composite hydro-mechanical properties in a statistical sense (Chen et al., 2008). The pore space can be modeled with cohesive zone elements (as a network of fractures) or with volume elements (as a porous solid with a shear modulus close to zero and with a permeability several orders of magnitude higher than that of the solid matrix around it). Alternatively, the FEM model can be designed to simulate fluid flow through a composite made of porous subdomains with different effective permeabilities as opposed to through the pore space itself. Displacements and pore pressures are solved at the nodes of the elements while stresses and porosity changes are calculated at integration points. If the nodes at the interface between subdomains are tied, fluid mass exchanges are calculated by assuming instantaneous equilibrium of pore pressures at the interface, i.e., infinite permeability orthogonal to the interface. Alternatively, interface elements can be inserted between the subdomains to reflect specific interface conductivity properties, including impermeable conditions. In all those FEM approaches, the field variables are not assumed to be uniform in each subdomain (or microstructure feature), which is why we call them “full-field methods”. Their main limitation is that mesh generation remains a challenge for complex microstructure topologies. As noted above, all numerical methods such as FVM and LBM assume a given flow regime and boundary condition set whose validity is clearly questionable in many instances. Fast Fourier Transform (FFT) - based methods are attractive for highly heterogeneous materials, because calculations are carried out on a regular grid and periodic boundary conditions minimize size effects. The numerical method established by Moulinec and Suquet (1998) is based on the FFT and on the introduction of a reference mate-

462 rial leading to the Lippmann-Schwinger (LS) equation (Suquet, 1990), which is then discretized.
463 Variational estimates of poromechanical and permeability properties were derived from the LS
464 equation (Bignonnet and Dormieux, 2013; Brisard and Ghabezloo, 2017). Full-field approaches
465 based on the LS equation typically perform better than a FEM (Lebensohn et al., 2008), but by
466 construction, FFT-based methods are better suited when the microstructure can be represented by
467 periodic cells. For example, the permeability of a periodic micro-porous medium saturated by a
468 viscous fluid was successfully calculated by using a FFT based computing method in which slip
469 boundary conditions at the pore wall are accounted for by introducing an interphase of infinitely
470 small thickness between the fluid and the solid (Monchiet et al., 2009). Later, a variational FFT-
471 based scheme based on the minimization of an energy Hashin–Shtrikman functional was proposed,
472 which allowed calculation of rigorous bounds of homogenized elastic properties in an energetically
473 consistent way (Brisard and Dormieux, 2010). This variational FFT approach makes it possible to
474 perform computations on large discretization grids (Brisard and Dormieux, 2012). The Hashin and
475 Shtrikman - based FFT scheme then inspired a numerical scheme to solve the Darcy flow problem
476 with periodic boundary conditions and calculate the rigorous bounds for the permeability tensor
477 (Bignonnet and Dormieux, 2014). One of the key issues for random composites is to find the size of
478 a statistically representative volume over which to calculate the effective properties. An automated
479 procedure to define the size of the discretized domain was recently proposed by Bignonnet (2020),
480 who found that the discretization of trial force fields on a regular grid permits the homogenization
481 of permeability from Stokes equations in voxel representations of the pore space and that energy
482 consistent discretizations deliver the most accurate results. Of note, the FFT based computing
483 method proposed in (Monchiet et al., 2009) to solve the Stokes equations was extended to doubly
484 porous solids constituted of two populations of pores which are different in size (Mezhoud et al.,
485 2020). The Darcy/Stokes coupled equations are solved by introducing the Brinkman equation
486 to represent the fluid exchange at the interface between the different subdomains. The fields of
487 velocity and traction are continuous across the interface, which is compatible with the use of the
488 Fourier series. Despite these advances, the reconstruction of a kinematically admissible velocity

489 field from the force field and the coupling between fluid flow and pore deformation remain open
490 issues, even in the most recent FFT-based methods.

491 *Pore network models*

492 Pore network models (PNMs) (Figure 1 (d)) can be used to relate the permeability tensor to
493 microstructure geometric properties. The original Kozeny-Carman model (Kozeny, 1927; Carman,
494 1937) considers that the pore fluid flows in a bundle of parallel pipes. Modified Kozeny-Carman
495 permeability formulas (Brace et al., 1968; Berryman and Blair, 1986; Petersen et al., 1996; Mavko
496 and Nur, 1997; Saar and Manga, 1999) indirectly relate average flow properties to tortuosity (e.g.,
497 through electrical conductivity). Statistical flow networks models (Dienes, 1982; Gueguen and
498 Dienes, 1989; Torquato, 1990; Schubnel et al., 2006; Fortin et al., 2011; Arson and Pereira, 2013)
499 and fractal network models (Tyler and Wheatcraft, 1990; Neuman, 1995; Pape et al., 1999) depend
500 on statistical microstructure descriptors. In the percolation theory (Stauffer and Aharony, 2018), the
501 characteristic flow path length is postulated, and transitions in flow regimes can only be predicted
502 if the probability of fluid saturation is known for each pore or crack. Although a non-uniform pore
503 arrangement produces hysteresis in retention curves (Romero et al., 1999; Wheeler et al., 2003;
504 Nuth and Laloui, 2008), most models that relate capillary pressure to pore size (Van Genuchten,
505 1980; Pereira and Arson, 2013) assume that the pore network is a bundle of pipes of constant cross
506 section, which are entirely filled with either wetting or non-wetting fluid.

507 More recent PNMs comprise pores (nodes) connected by constrictions or throats (edges).
508 A partitioning algorithm is required to identify individual pores if the pore space topology is
509 determined from micro computed tomography (Dong and Blunt, 2009; Taylor et al., 2015) or from
510 a DEM model (Reboul et al., 2010; van der Linden et al., 2018). Partitioning is non-trivial as
511 the void space is continuous and no partitioning algorithm can be wholly objective. For example,
512 Sufian et al. (2019) compare PNMs obtained using slightly different approaches to partitioning.
513 The model then considers mass balance for each pore in the system:

$$514 \quad \sum_{b=b_1}^{b_{Np}} Q_{ab} = 0 \quad (12)$$

515 where Q_{ab} is the fluid flow rate from pore a to pore b and $b_j, j = 1 - N_p$ are the ids of the N_p
 516 pores adjacent to pore a . Darcy's law effectively governs the flow from one pore to the next as

$$517 \quad Q_{ab} = G_{ab} \frac{p_a - p_b}{l_{ab}} \quad (13)$$

518 where G_{ab} is the hydraulic conductance of the throat connecting pores a and b ; the intrinsic
 519 conductance is given by $K_{ab} = \mu G_{ab}$. The proposed models to determine K_{ab} use a measure of the
 520 pore throat geometry and consider the Hagen-Poiseuille equation; expressions have been proposed
 521 by Bryant and Blunt (1992), Chareyre et al. (2012) and Patzek and Silin (2001).

522 *Mean-field homogenization methods*

523 In the homogenization theory, the Representative Elementary Volume (REV) is defined as the
 524 volume that has a characteristic size equal to the length of the shortest path that needs to be traveled
 525 inside the continuum to observe uniform variability of permeability properties. Typically, the REV
 526 is two orders of magnitude larger than the features of the microstructure that are expected to influence
 527 the permeability of the medium (e.g., pores, cracks). In mean-field homogenization approaches, the
 528 REV is divided into subdomains that each represent a microstructure feature (inclusion or matrix
 529 in which the inclusions are embedded in), and the field variables such as stress and pore pressure
 530 are uniform in each subdomain. This is in contrast to full-field methods, in which each feature or
 531 subdomain is discretized in space, and to PNMs, in which the concept of a matrix does not exist and
 532 the local gradient of pore pressure needs to be calculated at every constriction. Most permeability
 533 models based on mean-field homogenization approaches consider that Hagen-Poiseuille flow takes
 534 place in inclusions that represent penny-shaped cracks that are connected to a porous matrix and
 535 can intersect with one another. The matrix/inclusion interaction equation for mass transport is
 536 (Dormieux and Kondo, 2004):

$$537 \quad \nabla p(\mathbf{x}) = \mathbf{A}(\mathbf{x}) \cdot \langle \nabla p(\mathbf{x}) \rangle_D = \mathbf{A}(\mathbf{x}) \cdot \nabla \bar{P} \quad (14)$$

538 in which $\langle \dots \rangle_D$ is the space average over the domain D of the REV, $p(\mathbf{x})$ and \bar{P} are the local and
 539 REV scale pore pressure fields, and $\mathbf{A}(\mathbf{x})$ is the localization tensor (see Figure 3). Since the average
 540 velocity in the REV is equal to the average of the local velocity fields in the matrix and inclusions:

$$541 \quad \bar{\mathbf{k}} \cdot \nabla \bar{P} = \langle \mathbf{k}(\mathbf{x}) \cdot \nabla p(\mathbf{x}) \rangle_D \quad (15)$$

542 where $\bar{\mathbf{k}}$ and $\mathbf{k}(\mathbf{x})$ are the macroscopic (REV scale) and microscopic permeability tensors, respec-
 543 tively. The knowledge of $\mathbf{A}(\mathbf{x})$ yields the expression of the macroscopic permeability tensor:

$$544 \quad \bar{\mathbf{k}} = \langle \mathbf{k}(\mathbf{x}) \cdot \mathbf{A}(\mathbf{x}) \rangle_D \quad (16)$$

545 The expression of $\mathbf{A}(\mathbf{x})$ was found for Eshelby’s self-consistent scheme (Dormieux and Kondo,
 546 2004; Barthélemy, 2009; Chen et al., 2014) and for Ponte-Castaneda-Willis variational approach
 547 (Levasseur et al., 2013), which was used to predict the evolution of damage and permeability in
 548 the excavation damaged zone. More recently, Abdalrahman et al. (2015) used a self-consistent
 549 approach to express the localization tensor of interpenetrating cylindrical pore channels oriented
 550 randomly and interacting with impermeable spherical inclusions. The model was applied to the
 551 prediction of bone permeability, which is critical to fracture healing. The self-consistent model
 552 was then used to understand fluid flow - driven bone stimulation at three scales (Estermann and
 553 Scheiner, 2018).

554 *Permeability upscaling assisted by Artificial Intelligence (AI)*

555 In geomechanics, feature selection algorithms have been employed to identify sets of pore net-
 556 work and microstructural properties that optimally characterize permeability (van der Linden et al.,
 557 2016). Long-Short-Term-Memory (LSTM) neural networks have been used to optimize the expres-
 558 sions of the meso- and macro- effective stress and permeability tensors from offline simulations at
 559 the micro- and meso- scales, respectively (Wang and Sun, 2018). Hydraulic soil responses can also
 560 be generated from a neural network trained “off-line” with LBM results: mechanical constitutive
 561 updates are obtained from DEM simulations linked to a macroscopic dual-permeability model

562 (Wang and Sun, 2019b). Hybrid algorithms can predict either or both the mechanical and hydraulic
563 behavior of poroelastic media via constitutive models or via Machine Learning (ML) (Bahmani
564 and Sun, 2021). The ML algorithm solves an optimization problem (finding state variables as close
565 as possible to the data set) under constraints (momentum/mass balance equations, boundary con-
566 ditions). Reinforced learning allowed optimizing relationships between microstructure descriptors
567 and state variables (Wang and Sun, 2019a; Wang et al., 2019). The problem effectively is set as
568 a board game, in which a finite number of microstructure descriptors and state variables form the
569 nodes of a directed graph. The edges represent yet-unknown definitions or constitutive laws. The
570 probability of choosing an edge versus another is governed by a reward system. The reward is
571 calculated based on the accuracy of the constitutive model under constraints applied on the form
572 of the graph. Self-improving algorithms learn not only the constitutive laws, but also the optimal
573 setup, architecture, and hyper-parameters of the deep Convolutional Neural Networks (CNNs). The
574 deep reinforcement learning strategy is based on a Markov-Decision process and was applied to
575 predict path-dependent retention curves and anisotropic flow in micropores (Heider et al., 2021).

576 **Statistical physics approaches: from molecular to pore scale**

577 In order to bridge the gap between molecular dynamics and transport in porous networks, it is
578 necessary to: (i) characterize the structure of the porous medium and measure transport properties at
579 multiple scales, and (ii) couple experimental and numerical techniques to determine the expression
580 of the pore network permeability (or permeance) as a function of geometric and physical properties
581 established at multiple scales. In this context, statistical physics approaches – which were briefly
582 mentioned and introduced in this paper – are necessary to go beyond the classical Stokes equation
583 and include additional effects that induce deviations from Darcy’s law. Such a powerful framework
584 is also needed to provide a more general Darcy’s scheme, where the (intrinsic) permeability is
585 replaced with complex expressions for the general permeance.

586 *Geometric and transport properties at different scales*

587 To provide a robust scheme for transport upscaling, experimental structural data must be gathered
588 at each relevant scale. Such characterization methods, which are listed here in a non-exhaustive

589 fashion, allow probing additional effects that may be taken into account by operating at different
590 length scales. This includes techniques such as:

- 591 • Neutron or X-ray scattering at the \sim nm scale and beyond to probe adsorption and, in
592 general, all physical and physicochemical effects;
- 593 • Transmission Electron Microscopy (TEM), electron energy loss spectroscopy (EELS), Nan-
594 otomography (NanoT-SCAN) at the \sim 10 nm scale to probe pore shape effects;
- 595 • Focused ion beam and regular scanning electron microscopy (FIB-SEM and SEM) to probe
596 pore networks effects at the \sim 100 nm – 1 μ m scales;
- 597 • Computed tomography (CT-SCAN) and conventional microscopy at the macroscopic scales.

598 *Coupling experiments and simulations to find the expression of permeability*

599 Experimentally, many techniques allow probing the dynamics of fluids at different scales, e.g.,
600 relaxometry nuclear magnetic resonance (NMR), pulsed field gradient nuclear magnetic resonance
601 (PFGNMR), quasielastic neutron scattering (QENS), permeability measurements on core samples.
602 Similarly, several numerical methods can be used, such as molecular dynamics simulation (MD),
603 brownian dynamics (BD), dissipative particle dynamics (DPD), smoothed particle hydrodynamics
604 (SPH), lattice Boltzmann method (LBM), finite difference (FD) or finite volume (FV) reservoir
605 simulators. Connections between these different techniques could pave the way for robust upscaling,
606 whereby details of the structure-flow relationship are upscaled at the larger scale while keeping as
607 much information as possible. A key step along this roadmap is to collect transport data using other
608 techniques than permeability experiments. Indeed, this is needed as permeability (or permeance)
609 is the key quantity that should be modeled/predicted in the end so that it cannot be used directly
610 as a variable in the upscaling approach. For example, the collective diffusivity D_0 – which can
611 be assessed using techniques such as neutron scattering – is directly linked to the permeance K
612 [$K \sim D_0/\rho k_B T$] as noted earlier. Finally, we note that most upscaling techniques (e.g. pore
613 network models) and simulation techniques (e.g. LBM) – despite being established on robust
614 grounds – only include in an effective fashion the complex thermodynamics of the confined fluids

615 (adsorption, condensation, cavitation, etc). In contrast, other lattice models (e.g. Boğan et al.
616 (2015)) which account for the change in the chemical potential of the fluid upon stationary and/or
617 transient transport regimes allow one (in principle) to describe the coupling between fluid transport
618 and thermodynamics in complex porous media.

619 **PERSPECTIVES**

620 In engineering practice Darcy’s law is most often applied empirically to characterize transport
621 in complex porous media, where permeability is more a descriptor (a tensor when non-isotropic
622 materials are considered such as in sedimentary rocks and natural soils) rather than an intrinsic
623 physical constant of the medium. Even when a purely macro-scale, empirical approach is adopted,
624 it is challenging to accurately measure permeability in situ or in the laboratory (Cashman and
625 Preene, 2021). Simple expressions to determine the permeability k based on flow and material
626 parameters are currently unavailable for real, complex media (despite attempts to use physically
627 robust approaches such as mean-field methods).

628 This paper has highlighted that recent developments in numerical methods, imaging and ad-
629 vances in computational power enable us to take a new perspective on flow in porous media and
630 advance understanding of the fundamentals that underlie Darcy’s law. However, the paper has also
631 shown the benefit of using an analytical approach to explore the limitations of the applicability of
632 Darcy’s law in a very direct way. Starting from a consideration of flow in a single, cylindrical pore,
633 it has explored the applicability of Darcy’s law in different scenarios, including non-laminar flow
634 and non-advective flow. Working from this idealized model has enabled a reflection on the possible
635 definitions of permeability to extend Darcy’s law to poromechanical problems that involve strong
636 couplings with chemical and physical processes that occur at the pore scale and below. Using this
637 model, it can be shown that Darcy’s law is valid at all scales where the fluid can be modelled as a
638 continuum so long as the permeability is expressed as the correct function of geometric, chemical,
639 physical and mechanical parameters that fluid flow depends on. The exact dimensions at which the
640 continuum assumption applies depends on the fluid in question, the temperature and the pressure;
641 in general, for fluids, the continuum-discrete limit is approximately between 1nm and a few nm

642 (Bocquet and Charlaix, 2010). At the continuum scale, the value of considering a model of single
643 cylindrical pore, albeit a highly simplified abstraction of the situation in a real material, is that it
644 provides us with a clear basis to understand some of the limitations of the applicability of Darcy's
645 law.

646 In some situations though, expressing permeability as an appropriate function remains a chal-
647 lenge. To date, there are still many unexpected instances in which fluid velocity is not a linear
648 function of the gradient of pore pressure. From a geotechnical engineering perspective, for example,
649 there are some questions on the validity of Darcy's law in clays at low pressure gradients because
650 the structure of water in very small pores may be an issue (Hansbo, 2001). This is an issue that must
651 be addressed using simulations at the molecular scale (i.e. Molecular Dynamics) and it is timely to
652 harness this type of numerical model to look at this issue. We also need to better understand how
653 Darcy's law can be adapted to predict the infiltration of suspensions of bentonite/polymers used to
654 support boreholes and excavations: in these cases flow depends on the rheology of the fluid, which
655 is non-Newtonian (Ejezie et al. (2021); Darson-Balleur (2019)).

656 One of the key challenges is to characterize microstructure and measure transport properties at
657 multiple scales. To measure transport coefficients for different gases at various temperatures and
658 densities and establish accurate structure-property relationships, the impact of thermodynamic and
659 transport conditions onto fluid flow must be better understood. In particular, despite their broadly
660 acknowledged contribution to fluid flow, adsorption phenomena but also other thermodynamical
661 mechanisms (e.g. condensation, cavitation, pore blocking, etc.) are often overlooked as they are
662 treated in an effective, coarse-grained fashion. In this context, while these effects are often assumed
663 to occur only in very confining materials (e.g. nanoporous solids), they can have a strong impact
664 even when large pore materials are considered. For instance, even a vanishing amount of such
665 nanoporosity in the host medium can induce drastic macroscopic effects by changing locally the
666 thermodynamic and hydrodynamic boundary conditions imposed on the large porosity. Establishing
667 a robust connection between permeance (or hydraulic conductivity) and the variables of the problem
668 for simple pores is a prerequisite to any upscaling attempt to describe transport in complex, multi-

669 scale systems. Software development is still needed to decipher the scales of interest in fluid flow in
670 porous media. Key challenges remain, however there is now a real possibility of addressing some
671 complex fundamental questions using recent developments in numerical algorithms and advances
672 in computational power. This is an area which can be explored by appropriate application of direct
673 numerical simulation using either FVM or LBM and potentially including pore network modelling.

674 **DATA AVAILABILITY STATEMENT**

675 No data, models, or code were generated or used during the study.

676 **ACKNOWLEDGEMENTS**

677 Some of the arguments made in this paper are inspired from a formal debate held by COS and BC
678 and moderated by CA during the Biot-Bazant Conference on Engineering Mechanics and Physics
679 of Porous Materials, held June 1-3, 2021. A recording of the debate is available in (O’ Sullivan and
680 Coasne, 2021). We thank R. Hartkamp for providing the data for the molecular simulation snapshot
681 in Figure 1 (a). We also thank Mr. Tokio Morimoto who provided the images in Figures 1 (b) and
682 (d). Some of the arguments presented in this paper originated from Chloé Arson’s project “BRITE
683 Pivot Track: Micro-macro modeling of reactive flow and rock weathering enhanced by Artificial
684 Intelligence” which is funded by the U.S. National Science Foundation (NSF) under grant CMMI
685 # 2135584. The financial support from the NSF is gratefully acknowledged.

686 **REFERENCES**

- 687 Abdalrahman, T., Scheiner, S., and Hellmich, C. (2015). “Is trabecular bone permeability governed
688 by molecular ordering-induced fluid viscosity gain? arguments from re-evaluation of experi-
689 mental data in the framework of homogenization theory.” *Journal of theoretical biology*, 365,
690 433–444.
- 691 Arson, C. and Pereira, J.-M. (2013). “Influence of damage on pore size distribution and permeability
692 of rocks.” *International Journal for Numerical and Analytical Methods in Geomechanics*, 37(8),
693 810–831.

694 Bahmani, B. and Sun, W. (2021). “A kd-tree-accelerated hybrid data-driven/model-based approach
695 for poroelasticity problems with multi-fidelity multi-physics data.” *Computer Methods in Applied
696 Mechanics and Engineering*, 382, 113868.

697 Barrat, J. L. and Hansen, J. P. (2003). *Basic Concepts for Simple and Complex Liquids*. Cambridge
698 University Press.

699 Barthélémy, J.-F. (2009). “Effective permeability of media with a dense network of long and micro
700 fractures.” *Transport in porous media*, 76(1), 153–178.

701 Bear, J. (2018). *Modeling Phenomena of Flow and Transport in Porous Media*. Theory and
702 Applications of Transport in Porous Media. Springer International Publishing.

703 Berryman, J. G. and Blair, S. C. (1986). “Use of digital image analysis to estimate fluid permeability
704 of porous materials: Application of two-point correlation functions.” *Journal of applied Physics*,
705 60(6), 1930–1938.

706 Bignonnet, F. (2020). “Efficient fft-based upscaling of the permeability of porous media discretized
707 on uniform grids with estimation of rve size.” *Computer Methods in Applied Mechanics and
708 Engineering*, 369, 113237.

709 Bignonnet, F. and Dormieux, L. (2013). “Fft-based homogenization of permeability using a
710 hashin-shtrikman type variational framework.” *Poromechanics V: Proceedings of the Fifth Biot
711 Conference on Poromechanics*, 1245–1254.

712 Bignonnet, F. and Dormieux, L. (2014). “Fft-based bounds on the permeability of complex
713 microstructures.” *International Journal for Numerical and Analytical Methods in Geomechanics*,
714 38(16), 1707–1723.

715 Bird, R. B., Stewart, W. E., and Lightfoot, E. N. (2002). *Transport Phenomena (2nd edition)*. John
716 Wiley & Sons.

717 Blunt, M. J., Bijeljic, B., Dong, H., Gharbi, O., Iglauer, S., Mostaghimi, P., Paluszny, A., and
718 Pentland, C. (2013). “Pore-scale imaging and modelling.” *Advances in Water Resources*, 51,
719 197–216 35th Year Anniversary Issue.

720 Bocquet, L. and Charlaix, E. (2010). “Nanofluidics, from bulk to interfaces.” *Chem. Soc. Rev.*,
721 39(3), 1073–1095.

722 Boğan, A., Ulm, F.-J., Pellenq, R. J.-M., and Coasne, B. (2015). “Bottom-up model of adsorption
723 and transport in multiscale porous media.” *Phys. Rev. E*, 91(3), 032133.

724 Boutin, C., Auriault, J.-L., and Geindreau, C. (2010). *Homogenization of coupled phenomena in*
725 *heterogenous media*, Vol. 149. John Wiley & Sons.

726 Brace, W., Walsh, J., and Frangos, W. (1968). “Permeability of granite under high pressure.”
727 *Journal of Geophysical research*, 73(6), 2225–2236.

728 Brisard, S. and Dormieux, L. (2010). “Fft-based methods for the mechanics of composites: A
729 general variational framework.” *Computational Materials Science*, 49(3), 663–671.

730 Brisard, S. and Dormieux, L. (2012). “Combining galerkin approximation techniques with the prin-
731 ciple of hashin and shtrikman to derive a new fft-based numerical method for the homogenization
732 of composites.” *Computer Methods in Applied Mechanics and Engineering*, 217, 197–212.

733 Brisard, S. and Ghabezloo, S. (2017). “Variational estimates of the poroelastic coefficients.”
734 *Poromechanics VI*, 1266–1273.

735 Bryant, S. and Blunt, M. (1992). “Prediction of relative permeability in simple porous media.”
736 *Phys. Rev. A*, 46, 2004–2011.

737 Carman, P. C. (1937). “Fluid flow through granular beds.” *Trans. Inst. Chem. Eng.*, 15, 150–166.

738 Cashman, P. M. and Preene, M. (2021). *Groundwater Lowering in Construction A Practical Guide*
739 *to Dewatering*. CRC press, 3 edition.

740 Cedergren, H. (1967). *Seepage, Drainage and Flow Nets*. John Wiley & Sons.

741 Cedergren, H. (1997). *Seepage, Drainage, and Flow Nets*. John Wiley & Sons.

742 Chareyre, B., Cortis, A., and Catalano, E. e. a. (2012). “Pore-scale modeling of viscous flow and
743 induced forces in dense sphere packings.” *Transport in Porous Media*, 92, 473–493.

744 Chen, S.-H., Feng, X.-M., and Isam, S. (2008). “Numerical estimation of rev and permeability tensor
745 for fractured rock masses by composite element method.” *International journal for numerical
746 and analytical methods in geomechanics*, 32(12), 1459–1477.

747 Chen, Y., Hu, S., Zhou, C., and Jing, L. (2014). “Micromechanical modeling of anisotropic damage-
748 induced permeability variation in crystalline rocks.” *Rock mechanics and rock engineering*, 47(5),
749 1775–1791.

750 Coasne, B. (2016). “Multiscale adsorption and transport in hierarchical porous materials.” *New J.
751 Chem.*, 40, 4078–4094.

752 Darcy, H. (1856). *Les fontaines publiques de la ville de Dijon : exposition et application des
753 principes à suivre et des formules à employer dans les questions de distribution d’eau*. Victor
754 Dalmont, Paris.

755 Darson-Balleur, S., e. a. (2019). *Guide to Support Fluids for Deep Foundations*. EFFC, DFI.

756 Dienes, J. K. (1982). “Permeability, percolation and statistical crack mechanics.” *The 23rd US
757 Symposium on Rock Mechanics (USRMS)*, OnePetro.

758 Dong, H. and Blunt, M. J. (2009). “Pore-network extraction from micro-computerized-tomography
759 images.” *Phys. Rev. E*, 80, 036307.

760 Dormieux, L. and Kondo, D. (2004). “Approche micromécanique du couplage perméabilité–
761 endommagement.” *Comptes Rendus Mécanique*, 332(2), 135–140.

762 Ejezie, J. O., Jefferis, S. A., Lam, C., Sedighi, M., and Ahmad, S. M. (2021). “Permeation behaviour
763 of phpa polymer fluids in sand.” *Géotechnique*, 71(7), 561–570.

764 Estermann, S.-J. and Scheiner, S. (2018). “Multiscale modeling provides differentiated insights to
765 fluid flow-driven stimulation of bone cellular activities.” *Frontiers in Physics*, 6, 76.

766 Falk, K., Coasne, B., Pellenq, R., Ulm, F.-J., and Bocquet, L. (2015). “Subcontinuum mass
767 transport of condensed hydrocarbons in nanoporous media.” *Nature Communications*, 6, 6949.

768 Fortin, J., Stanchits, S., Vinciguerra, S., and Guéguen, Y. (2011). “Influence of thermal and
769 mechanical cracks on permeability and elastic wave velocities in a basalt from mt. etna volcano
770 subjected to elevated pressure.” *Tectonophysics*, 503(1-2), 60–74.

771 Gueguen, Y. and Dienes, J. (1989). “Transport properties of rocks from statistics and percolation.”
772 *Mathematical geology*, 21(1), 1–13.

773 Hansbo, S. (2001). “Consolidation equation valid for both darcian and non-darcian flow.” *Géotech-*
774 *nique*, 51(1), 51–54.

775 Hartkamp, R., Siboulet, B., Dufrêche, J.-F., and Coasne, B. (2015). “Ion-specific adsorption and
776 electroosmosis in charged amorphous porous silica.” *Phys. Chem. Chem. Phys.*, 17, 24683–
777 24695.

778 Heider, Y., Suh, H. S., and Sun, W. (2021). “An offline multi-scale unsaturated poromechanics model
779 enabled by self-designed/self-improved neural networks.” *International Journal for Numerical
780 and Analytical Methods in Geomechanics*.

781 Ineson, J. (1956). “Darcy’s law and the evaluation of permeability..” *International Association of
782 Hydrological Sciences, Symposia Darcy, Dijon. Publication 41*, 165–172.

783 Kärger, J., Ruthven, D. M., and Theodorou, D. N. (2012). *Diffusion in Nanoporous Materials*. John
784 Wiley & Sons (April).

785 Knappett, J. and Craig, R. (2012). *Craig's Soil Mechanics*. CRC Press.

786 Knight, C., O'Sullivan, C., van Wachem, B., and Dini, D. (2020). "Computing drag and interac-
787 tions between fluid and polydisperse particles in saturated granular materials." *Computers and*
788 *Geotechnics*, 117, 103210.

789 Kozeny, J. (1927). "Über kapillare leitung der wasser in boden." *Royal Academy of Science, Vienna,*
790 *Proc. Class I*, 136, 271–306.

791 Lebensohn, R. A., Brenner, R., Castelnau, O., and Rollett, A. D. (2008). "Orientation image-
792 based micromechanical modelling of subgrain texture evolution in polycrystalline copper." *Acta*
793 *Materialia*, 56(15), 3914–3926.

794 Levasseur, S., Collin, F., Charlier, R., and Kondo, D. (2013). "A micro–macro approach of
795 permeability evolution in rocks excavation damaged zones." *Computers and Geotechnics*, 49,
796 245–252.

797 Mavko, G. and Nur, A. (1997). "The effect of a percolation threshold in the kozeny-carman
798 relation." *Geophysics*, 62(5), 1480–1482.

799 Mc Quarrie, D. A. (2000). *Statistical Mechanics*. Harper & Row.

800 Mezhoud, S., Monchiet, V., Bornert, M., and Grande, D. (2020). "Computation of macroscopic per-
801 meability of doubly porous media with fft based numerical homogenization method." *European*
802 *Journal of Mechanics-B/Fluids*, 83, 141–155.

803 Mitchell, J. and Soga, K. (2005). *Fundamentals of Soil Behavior*. John Wiley & Sons.

804 Monchiet, V., Bonnet, G., and Lauriat, G. (2009). "A fft-based method to compute the permeability
805 induced by a stokes slip flow through a porous medium." *Comptes Rendus Mécanique*, 337(4),
806 192–197.

807 Moulinec, H. and Suquet, P. (1998). “A numerical method for computing the overall response of
808 nonlinear composites with complex microstructure.” *Computer methods in applied mechanics
809 and engineering*, 157(1-2), 69–94.

810 Neuman, S. P. (1995). “On advective transport in fractal permeability and velocity fields.” *Water
811 Resources Research*, 31(6), 1455–1460.

812 Nield, D. A. and Bejan, A. (2006). *Convection in Porous Media*. Springer.

813 Nuth, M. and Laloui, L. (2008). “Advances in modelling hysteretic water retention curve in
814 deformable soils.” *Computers and Geotechnics*, 35(6), 835–844.

815 O’ Sullivan, C. and Coasne, B. (2021). “Debate: Darcy’s law is meaningless for flow within
816 individual pores.” *Biot Bazant Conference on Engineering Mechanics and Physics of Porous
817 Materials*.

818 Obliger, A., Pellenq, R., Ulm, F.-J., and Coasne, B. (2016). “Free Volume Theory of Hydrocarbon
819 Mixture Transport in Nanoporous Materials.” *J. Phys. Chem. Lett.*, 7(19), 3712–3717.

820 Onsager, L. (1931). “Reciprocity relations in irreversible thermodynamics. i.” *Phys. Rev.*, 37,
821 405–426.

822 Pape, H., Clauser, C., and Iffland, J. (1999). “Permeability prediction based on fractal pore-space
823 geometry.” *Geophysics*, 64(5), 1447–1460.

824 Pathirannahalage, S. K., Meftahi, N., Elbourne, A., Weiss, A. C. G., McConville, C. F., Padua, A.,
825 Winkler, D. A., Costa Gomes, M., Greaves, T. L., Le, T. C., Besford, Q. A., and Christofferson,
826 A. J. (2021). “Systematic comparison of the structural and dynamic properties of commonly
827 used water models for molecular dynamics simulations.” *Journal of Chemical Information and
828 Modeling*, 61(9), 4521–4536 PMID: 34406000.

829 Patzek, T. and Silin, D. (2001). “Shape factor and hydraulic conductance in noncircular capillaries:
830 I. one-phase creeping flow.” *Journal of Colloid and Interface Science*, 236(2), 295–304.

831 Pereira, J.-M. and Arson, C. (2013). “Retention and permeability properties of damaged porous
832 rocks.” *Computers and Geotechnics*, 48, 272–282.

833 Petersen, L. W., Moldrup, P., Jacobsen, O. H., and Rolston, D. E. (1996). “Relations between
834 specific surface area and soil physical and chemical properties.” *Soil Science*, 161(1), 9–21.

835 Reboul, N., Vincens, E., and Cambou, B. (2010). “A computational procedure to assess the
836 distribution of constriction sizes for an assembly of spheres.” *Computers and Geotechnics*,
837 37(1), 195–206.

838 Romero, E., Gens, A., and Lloret, A. (1999). “Water permeability, water retention and microstruc-
839 ture of unsaturated compacted boom clay.” *Engineering Geology*, 54(1-2), 117–127.

840 Saar, M. O. and Manga, M. (1999). “Permeability-porosity relationship in vesicular basalts.”
841 *Geophysical Research Letters*, 26(1), 111–114.

842 Sanvitale, N., Zhao, B., Bowman, E., and O’Sullivan, C. (2022). “Particle-scale observation of
843 seepage flow in granular soils using piv and cfd.” *Géotechnique*, 1–57.

844 Schubnel, A., Benson, P. M., Thompson, B. D., Hazzard, J. F., and Young, R. P. (2006). “Quanti-
845 fying damage, saturation and anisotropy in cracked rocks by inverting elastic wave velocities.”
846 *Rock damage and fluid transport, part I*, Springer, 947–973.

847 Smith, P., Simm, J., Gains, R., Mars, S. S., Perlea, M., and Wielputz, M. (2013). “Chapter 9
848 design.” *The International Levee Handbook*, CIRIA.

849 Stauffer, D. and Aharony, A. (2018). *Introduction to percolation theory*. CRC press.

850 Su, T.-C. (2018). “Exploring semi-solid alloy deformation with discrete element method simulations
851 and synchrotron radiography.” Ph.D. thesis, Imperial College London, Imperial College London.

852 Sufian, A., Knight, C., O’Sullivan, C., van Wachem, B., and Dini, D. (2019). “Ability of a pore
853 network model to predict fluid flow and drag in saturated granular materials.” *Computers and*
854 *Geotechnics*, 110, 344–366.

855 Sun, W. and Wong, T.-f. (2018). “Prediction of permeability and formation factor of sandstone with
856 hybrid lattice boltzmann/finite element simulation on microtomographic images.” *International*
857 *Journal of Rock Mechanics and Mining Sciences*, 106, 269–277.

858 Suquet, P. (1990). “Une méthode simplifiée pour le calcul des propriétés élastiques de matéri-
859 aux hétérogènes à structure périodique.” *Comptes rendus de l’Académie des sciences. Série 2,*
860 *Mécanique, Physique, Chimie, Sciences de l’univers, Sciences de la Terre*, 311(7), 769–774.

861 Talon, L., Bauer, D., Gland, N., Youssef, S., Auradou, H., and Ginzburg, I. (2012). “Assessment
862 of the two relaxation time lattice-boltzmann scheme to simulate stokes flow in porous media.”
863 *Water Resources Research*, 48(4).

864 Taylor, H., O’Sullivan, C., and Sim, W. (2015). “A new method to identify void constrictions in
865 micro-ct images of sand.” *Computers and Geotechnics*, 69, 279–290.

866 Taylor, H. F., O’Sullivan, C., Sim, W. W., and Carr, S. J. (2017). “Sub-particle-scale investigation
867 of seepage in sands.” *Soils and Foundations*, 57(3), 439–452.

868 Torquato, S. (1990). “Relationship between permeability and diffusion-controlled trapping constant
869 of porous media.” *Physical review letters*, 64(22), 2644.

870 Tyler, S. W. and Wheatcraft, S. W. (1990). “Fractal processes in soil water retention.” *Water*
871 *Resources Research*, 26(5), 1047–1054.

872 van der Linden, J. H., Narsilio, G. A., and Tordesillas, A. (2016). “Machine learning framework
873 for analysis of transport through complex networks in porous, granular media: A focus on
874 permeability.” *Physical Review E*, 94(2), 022904.

875 van der Linden, J. H., Sufian, A., Narsilio, G. A., Russell, A. R., and Tordesillas, A. (2018).
876 “A computational geometry approach to pore network construction for granular packings.”
877 *Computers & Geosciences*, 112, 133–143.

- 878 Van Genuchten, M. T. (1980). “A closed-form equation for predicting the hydraulic conductivity
879 of unsaturated soils.” *Soil science society of America journal*, 44(5), 892–898.
- 880 Wang, K. and Sun, W. (2018). “A multiscale multi-permeability poroplasticity model linked by
881 recursive homogenizations and deep learning.” *Computer Methods in Applied Mechanics and
882 Engineering*, 334, 337–380.
- 883 Wang, K. and Sun, W. (2019a). “Meta-modeling game for deriving theory-consistent,
884 microstructure-based traction–separation laws via deep reinforcement learning.” *Computer Meth-
885 ods in Applied Mechanics and Engineering*, 346, 216–241.
- 886 Wang, K. and Sun, W. (2019b). “An updated lagrangian lbm–dem–fem coupling model for
887 dual-permeability fissured porous media with embedded discontinuities.” *Computer Methods
888 in Applied Mechanics and Engineering*, 344, 276–305.
- 889 Wang, K., Sun, W., and Du, Q. (2019). “A cooperative game for automated learning of elasto-
890 plasticity knowledge graphs and models with ai-guided experimentation.” *Computational Me-
891 chanics*, 64(2), 467–499.
- 892 Wheeler, S., Sharma, R., and Buisson, M. (2003). “Coupling of hydraulic hysteresis and stress–
893 strain behaviour in unsaturated soils.” *Géotechnique*, 53(1), 41–54.
- 894 Zhang, C. and Lu, N. (2018). “What is the range of soil water density? critical reviews with a
895 unified model.” *Reviews of Geophysics*, 56(3), 532–562.
- 896 Zhao, B. and O’Sullivan, C. (2022). “Fluid particle interaction in packings of monodisperse angular
897 particles.” *Powder Technology*, 395, 133–148.
- 898 Ziarani, A. S. and Aguilera, R. (2012). “Knudsen’s Permeability Correction for Tight Porous
899 Media.” *Transp Porous Med*, 91(1), 239–260.

900 **List of Tables**

901 1 Typical values for hydraulic conductivity (also called coefficient of permeability in
902 the geotechnical literature) for geomaterials developed with reference to Cashman
903 and Preene (2021) 38

TABLE 1. Typical values for hydraulic conductivity (also called coefficient of permeability in the geotechnical literature) for geomaterials developed with reference to Cashman and Preene (2021)

| Soil Type | Hydraulic conductivity $K' = k\rho g/\eta$ (K'_{ij} in ms^{-1}) | Qualitative / engineering description |
|---|---|--|
| Intact clays | $< 10^{-9}$ | Practically impermeable |
| Fissured or laminated clays | 10^{-9} to 10^{-7} | Very low |
| Sandy silts, very silty fine sands, and laminated or mixed strata of silt/sand/clay | 10^{-8} to 10^{-5} | Low to very low |
| Silty sands | 10^{-6} to 10^{-4} | Low |
| Fine and medium sands | 10^{-4} to 5×10^{-4} | Moderate to low |
| Clean sand and sand/gravel mixtures | 5×10^{-4} to 10^{-3} | High to moderate |
| Clean gravels | $> 10^{-3}$ | High |

904
905
906
907
908
909
910
911
912
913
914
915
916
917
918
919
920
921

List of Figures

- 1 Flow in porous media at multiple scales. (a) Schematic of molecular model of water (Hartkamp et al., 2015) (b) Illustration of the pore space in which flow occurs, modeled with FVM (Finite Volume Method) (Image by Mr. T. Morimoto). (c) Flow velocity field in this pore space, e.g. calculated by LBM (Lattice Boltzman Method) after (Su, 2018). (d) Pore network model (Image by Mr. T. Morimoto). (e) Flow net which is a graphical solution to the Laplace equation (derived using Darcy’s law where soil is considered as a continuum) (Knappett and Craig (2012); Cedergren (1997)). 41

- 2 Sub-pore scale modeling of fluid flow. (a) Poiseuille flow for a fluid made of molecules (red spheres) in a slit pore of width D (stone like aspect). The fluid flow obeys a parabolic velocity profile upon applying a pressure gradient ∇P parallel to the pore surfaces. x and r are the direction parallel and perpendicular to the pore surface. (b) Depending on the so-called surface boundary condition, $v_x(r) \sim 0$ at the pore surface (no-slip boundary condition, left panel) or $v_x(r) \neq 0$ (slip boundary condition, right panel). In the latter case, slippage occurs with a slip length b which corresponds to the distance at which the extrapolated velocity profile reaches zero: $-b\partial v_x/\partial r = v_x$ 42

922 3 Principle of permeability homogenization according to Eshelby’s theory. **(1) Av-**
923 **eraging.** In the case of a domain D that is subjected to a linear pore pressure in
924 the far field ($P_\infty(\mathbf{x}) = \mathbf{x} \cdot \nabla P_\infty$) and that contains a heterogeneity Ω , the gradient
925 of pressure in the matrix $D \setminus \Omega$, noted $\nabla p_0(\mathbf{x})$, is equal to the uniform gradient
926 of pressure applied at the far-field boundary (∇P_∞) plus the gradient of a distur-
927 bance pressure field ($\nabla p_d(\mathbf{x})$), due to the presence of the heterogeneity. Similarly,
928 the gradient of pressure in the heterogeneity ($\nabla p_i(\mathbf{x})$) is equal to $\nabla P_\infty + \nabla p_d(\mathbf{x})$.
929 Additionally, the flow rates in the matrix ($\bar{\mathbf{v}}_0(\mathbf{x})$) and in the heterogeneity ($\bar{\mathbf{v}}_i(\mathbf{x})$)
930 are related to $p_0(\mathbf{x})$ and $p_i(\mathbf{x})$ respectively, via Darcy’s law. In Eshelby’s theory,
931 the gradients of the local fields of pressure are related to the average gradient of
932 pressure in the domain D by localization tensors ($\mathbf{A}_0(\mathbf{x})$ for the matrix, $\mathbf{A}_i(\mathbf{x})$ for
933 the heterogeneity), which depend on the shape of the heterogeneities. **(2) Solving**
934 **for local field variables.** The pressure field in the matrix, $p_0(\mathbf{x})$, is calculated by
935 solving a cavity expansion problem, in which $P_\infty(\mathbf{x})$ is applied in the far field and
936 $p_i(\mathbf{x})$ is applied at the matrix/heterogeneity interface. The field $p_i(\mathbf{x})$ is calculated
937 by the equivalent inclusion method, in which the heterogeneity Ω is assigned the
938 same permeability as the matrix $D \setminus \Omega$. To compensate the error made in the esti-
939 mation of the flow rate in the heterogeneity, a gradient of eigenpressure ($\nabla p_i^*(\mathbf{x})$)
940 is subtracted from the local gradient of pressure ($\nabla p_i(\mathbf{x})$) in Darcy’s law. It can be
941 shown that the gradient of eigenpressure field is uniform in Ω and that there is a
942 linear relationship between the gradient of the disturbance pressure field ($\nabla p_d(\mathbf{x})$)
943 and the gradient of the eigenpressure field (∇p_i^*). The relationship between the
944 two holds in the so-called Eshelby tensor \mathbb{S}_i , which itself, depends on the Green’s
945 tensor and on the localization tensors ($\mathbf{A}_0(\mathbf{x})$, $\mathbf{A}_i(\mathbf{x})$). **(3) Generalization.** For a
946 set of heterogeneities, assumptions on the interactions between heterogeneities are
947 introduced to close the formulation. 43

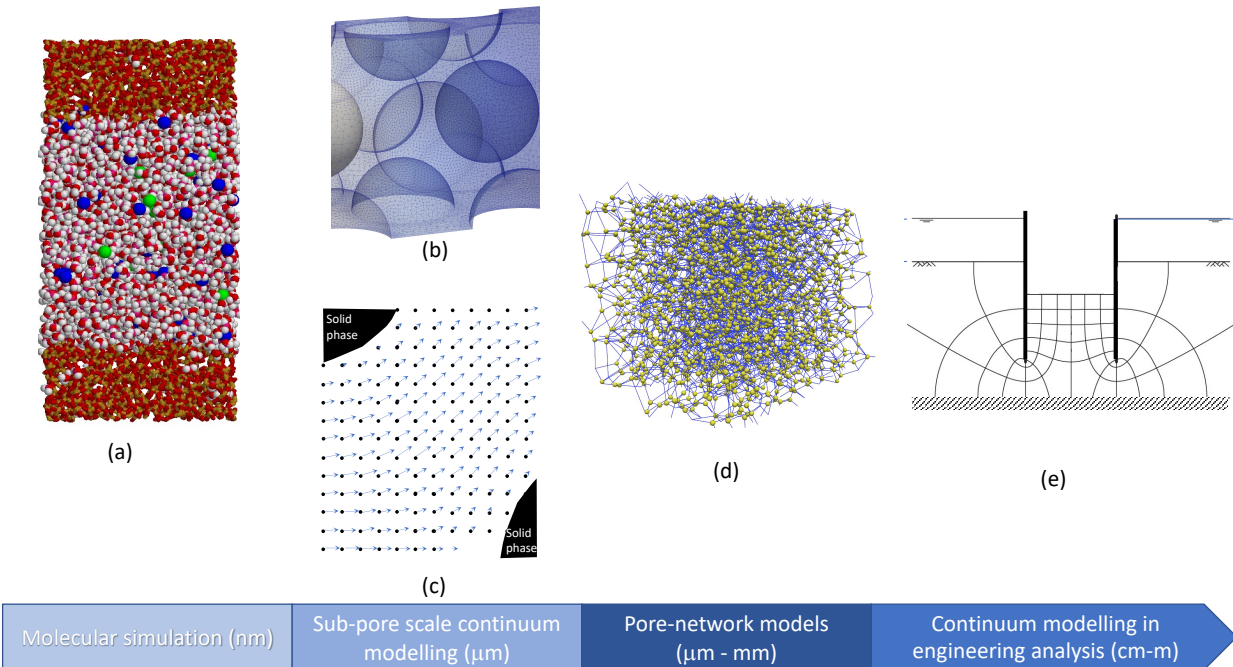


Fig. 1. Flow in porous media at multiple scales. (a) Schematic of molecular model of water (Hartkamp et al., 2015) (b) Illustration of the pore space in which flow occurs, modeled with FVM (Finite Volume Method) (Image by Mr. T. Morimoto). (c) Flow velocity field in this pore space, e.g. calculated by LBM (Lattice Boltzman Method) after (Su, 2018). (d) Pore network model (Image by Mr. T. Morimoto). (e) Flow net which is a graphical solution to the Laplace equation (derived using Darcy's law where soil is considered as a continuum) (Knappett and Craig (2012); Cedergren (1997)).

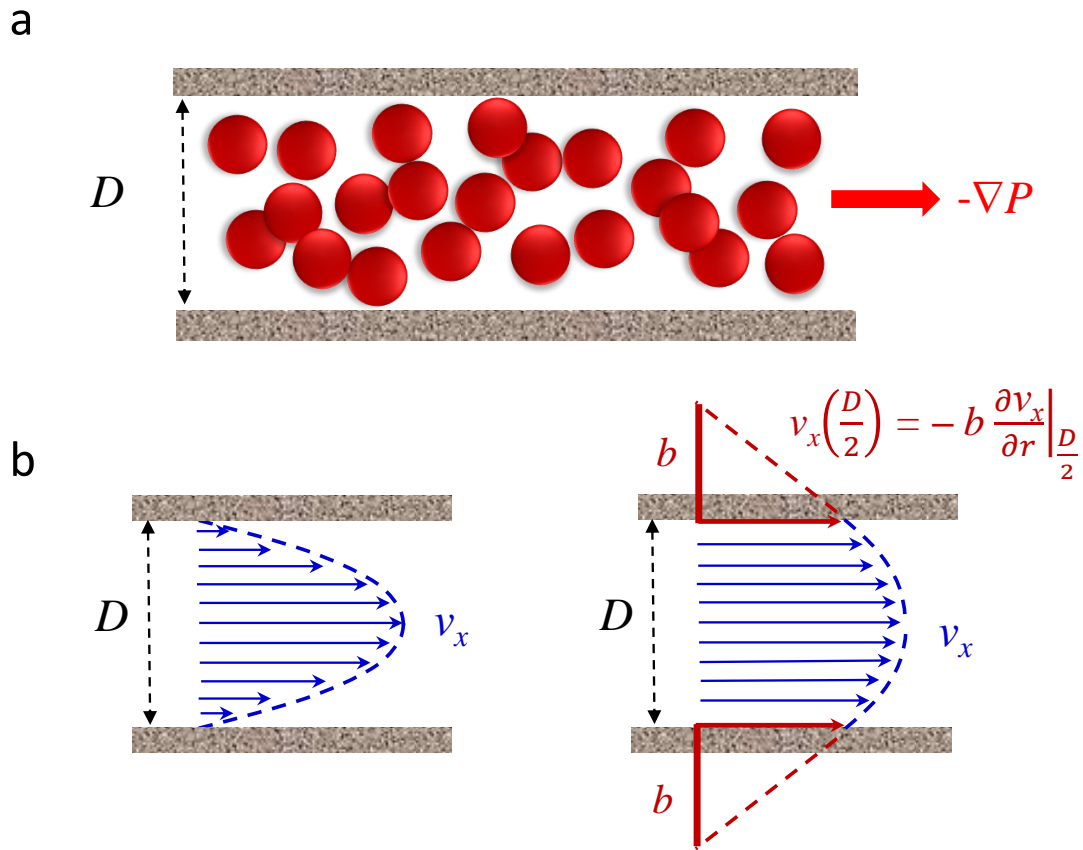
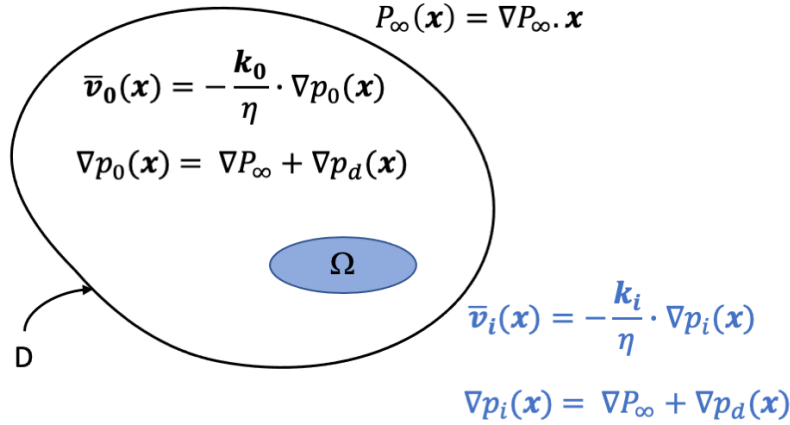


Fig. 2. Sub-pore scale modeling of fluid flow. (a) Poiseuille flow for a fluid made of molecules (red spheres) in a slit pore of width D (stone like aspect). The fluid flow obeys a parabolic velocity profile upon applying a pressure gradient ∇P parallel to the pore surfaces. x and r are the direction parallel and perpendicular to the pore surface. (b) Depending on the so-called surface boundary condition, $v_x(r) \sim 0$ at the pore surface (no-slip boundary condition, left panel) or $v_x(r) \neq 0$ (slip boundary condition, right panel). In the latter case, slippage occurs with a slip length b which corresponds to the distance at which the extrapolated velocity profile reaches zero: $-b \partial v_x / \partial r = v_x$.



1. Introduce assumptions on microstructure:

$$\left. \begin{aligned} \nabla p_0(\mathbf{x}) &= \mathbf{A}_0(\mathbf{x}) \cdot \langle \nabla p(\mathbf{x}) \rangle_D \\ \nabla p_i(\mathbf{x}) &= \mathbf{A}_i(\mathbf{x}) \cdot \langle \nabla p(\mathbf{x}) \rangle_D \end{aligned} \right\} \bar{\mathbf{k}} = \langle \mathbf{k}(\mathbf{x}) \cdot \mathbf{A}(\mathbf{x}) \rangle_D$$

2. Solve using Eshelby's equivalent inclusion method:

$$\bar{\mathbf{v}}_i(\mathbf{x}) = -\frac{\mathbf{k}_0}{\eta} \cdot [\nabla p_i(\mathbf{x}) - \nabla p_i^*]$$

$$\nabla p_d(\mathbf{x}) = \mathbb{S}_i : \nabla p_i^* \quad \mathbb{S}_i = f(\mathbf{A}_0, \mathbf{A}_i)$$

Fig. 3. Principle of permeability homogenization according to Eshelby's theory. **(1) Averaging.** In the case of a domain D that is subjected to a linear pore pressure in the far field ($P_\infty(\mathbf{x}) = \mathbf{x} \cdot \nabla P_\infty$) and that contains a heterogeneity Ω , the gradient of pressure in the matrix $D \setminus \Omega$, noted $\nabla p_0(\mathbf{x})$, is equal to the uniform gradient of pressure applied at the far-field boundary (∇P_∞) plus the gradient of a disturbance pressure field ($\nabla p_d(\mathbf{x})$), due to the presence of the heterogeneity. Similarly, the gradient of pressure in the heterogeneity ($\nabla p_i(\mathbf{x})$) is equal to $\nabla P_\infty + \nabla p_d(\mathbf{x})$. Additionally, the flow rates in the matrix ($\bar{\mathbf{v}}_0(\mathbf{x})$) and in the heterogeneity ($\bar{\mathbf{v}}_i(\mathbf{x})$) are related to $p_0(\mathbf{x})$ and $p_i(\mathbf{x})$ respectively, via Darcy's law. In Eshelby's theory, the gradients of the local fields of pressure are related to the average gradient of pressure in the domain D by localization tensors ($\mathbf{A}_0(\mathbf{x})$ for the matrix, $\mathbf{A}_i(\mathbf{x})$ for the heterogeneity), which depend on the shape of the heterogeneities. **(2) Solving for local field variables.** The pressure field in the matrix, $p_0(\mathbf{x})$, is calculated by solving a cavity expansion problem, in which $P_\infty(\mathbf{x})$ is applied in the far field and $p_i(\mathbf{x})$ is applied at the matrix/heterogeneity interface. The field $p_i(\mathbf{x})$ is calculated by the equivalent inclusion method, in which the heterogeneity Ω is assigned the same permeability as the matrix $D \setminus \Omega$. To compensate the error made in the estimation of the flow rate in the heterogeneity, a gradient of eigenpressure ($\nabla p_i^*(\mathbf{x})$) is subtracted from the local gradient of pressure ($\nabla p_i(\mathbf{x})$) in Darcy's law. It can be shown that the gradient of eigenpressure field is uniform in Ω and that there is a linear relationship between the gradient of the disturbance pressure field ($\nabla p_d(\mathbf{x})$) and the gradient of the eigenpressure field (∇p_i^*). The relationship between the two holds in the so-called Eshelby tensor \mathbb{S}_i , which itself, depends on the Green's tensor and on the localization tensors ($\mathbf{A}_0(\mathbf{x})$, $\mathbf{A}_i(\mathbf{x})$). **(3) Generalization.** For a set of heterogeneities, assumptions on the interactions between heterogeneities are introduced to close the formulation.